Battery Energy

WILEY

RESEARCH ARTICLE OPEN ACCESS

Microwave-Assisted Recycling of Lithium-Ion Batteries: Linking Process Optimization to Volatile Organic Compounds and Fluorinated Gases Emission Mitigation

Alberto Mannu[1] | Giacomo Luigi Petretto[2] | Erica Pietrobelli[1] | Alessandro Bonometti[1] | Maria Enrica Di Pietro[3] | Andrea Mele[3] | Laura Eleonora Depero[1] | Elza Bontempi[1]

[1]INSTM and Chemistry for Technologies Laboratory, Department of Mechanical and Industrial Engineering, University of Brescia, Brescia, Italy | [2]Department of Medical, Surgery and Pharmacy, University of Sassari Viale San Pietro, Sassari, Italy | [3]Department of Chemistry, Materials and Chemical Engineering "Giulio Natta", Politecnico di Milano, Milano, Italy

Correspondence: Alberto Mannu (alberto.mannu@unibs.it)

Received: 13 November 2025 | **Revised:** 13 January 2026 | **Accepted:** 19 January 2026

Funding: Ministero dell'Universita e della Ricerca, Grant/Award Numbers: D73C24000220001, D73C22001250001

Keywords: black mass | Design of Experiments | microwave treatment | multinuclear magnetic resonance | volatile organic compounds

ABSTRACT

This work investigates the volatile fraction released from black mass (BM) obtained from spent lithium-ion batteries subjected to microwave (MW) thermal treatment. MW processing is emerging as an alternative to conventional pyrometallurgy for improving energy efficiency and recovery of critical metals such as lithium, yet the associated emission profile remains poorly characterized. However, the studies of the emissions associated with these treatments are quite limited. Here, a multilevel full factorial Design of Experiments is applied for the first time to evaluate the influence of MW power, exposure time, and BM mass on heating dynamics and lithium extraction efficiency. Volatile organic compounds generated during MW processing are identified by headspace solid-phase microextraction coupled to gas chromatography–mass spectrometry (HS-SPME/GC-MS), showing a complex mixture of aliphatic and aromatic hydrocarbons, carbonate esters, and phosphorus- and fluorine-containing species. Multinuclear NMR spectroscopy (^{1}H, ^{7}Li, ^{19}F, ^{31}P) confirms the presence of electrolyte-derived residues such as Li^{+}, PF_6^{-}, and phosphate esters. The combined analytical approach clarifies degradation pathways during MW heating and highlights the need to monitor and mitigate the formation of potentially hazardous volatile species in future MW-assisted recycling processes. Statistical models reveal that the time to reach 600°C and the maximum temperature depend primarily on power and exposure time, while Li recovery is governed by BM mass and its interaction with power.

1 | Introduction

The surge in lithium-ion battery (LIB) production for EVs and storage is straining raw material supply. By 2040, lithium demand could reach 0.8 Mt (up from 0.1 Mt in 2021), cobalt 0.5 Mt (from 0.17 Mt), and nickel 3.5 Mt (from 2.7 Mt), while manganese stays far below its 20 Mt supply. Recycling could provide over half of future lithium and nickel needs and even exceed cobalt demand, reducing reliance on concentrated mining, where 90% of lithium and 73% of cobalt come from only a few countries [1]. This underpins the strategic role of waste mining, recovering Li, Co, Ni, and graphite from end-of-life LIBs, to reduce reliance on primary extraction and stabilize supply chains [2]. Current waste mining processes are based on the treatment of milled spent batteries, which provide a black powder named black mass (BM) [3]. BM is a heterogeneous material rich in strategic metals such as Li, Co, Ni, and Mn, depending on the specific cathodes, accompanied by variable amounts of P, Al, Si, Ca, F, organic compounds, and other

minor chemicals [4]. Industrial recycling is focused on the recovery of the main metals by pyrometallurgical or hydrometallurgical approaches. Pyrometallurgical recycling generally employs high-temperature smelting in the 1400°C–1700°C range to reduce metal oxides and melt alloys, often following a thermal pretreatment to remove organics (e.g., pyrolysis at 700°C to remove binders/plastics) [5]. The extreme temperatures enable short process flows but necessitate significant energy input and extensive gas cleaning (off-gas scrubbing) to handle volatilized species [6]. Moreover, hydrometallurgy enables selective metal recovery through acidic leaching and can generate gaseous emissions. [7].

Regarding gaseous emissions, recent studies on industrial LIB recycling revealed that the pyrolysis and leaching stages release complex mixtures of volatile organic compounds (VOCs), halogenated hydrocarbons, and fluorinated gases [8]. Typical species include ethyl acetate due to mechanical treatments. Chloromethane and 1,2-dichloroethane are formed during the alkali leaching, and acetaldehyde and cyclohexane are due to the acid leaching step [8]. The main components identified in the pyrolysis step are 1,2-dichloroethane and epichlorohydrin. Furthermore, the PVDF binder in cathodes has been identified as a major source of fluorine-containing gases, such as HF, CH_3F, $C_2H_2F_2$, and $C_6H_3F_3$, during thermal decomposition [9]. These fluorinated emissions arise even at relatively low pyrolysis temperatures (350°C–500°C) and are linked to electrophilic attacks on C—C and C—F bonds, following a random nucleation–growth mechanism. Therefore, monitoring fluorinated volatiles is critical, as their presence indicates the onset of PVDF degradation and binder detachment.

In the last years, microwave (MW) thermal treatment has emerged as a promising alternative/adjunct treatment for BM, a powder containing graphite, cathode oxides, and organics. MW processing can achieve target temperatures within minutes, altering decomposition kinetics versus conventional heating. On LCO-rich BM, Cornelio et al. [10] report > 80% Li recovery after only 5 min at 600 W, leveraging enhanced coupling of carbonaceous fractions and magnetic components to boost absorber temperature. On a mixed industrial NMC622 shredder (including foils and separator), Stallmeister et al. [9] systematically map the influence of power, time, and atmosphere, demonstrate rapid processing, and carry out a scale-up, demonstrating MW treatment transferability beyond laboratory scale.

Despite increasing attention to MW processing of BM, reproducible control of heating profiles remains unresolved due to BM heterogeneity and complex interactions between the MWs and the material [11–14].

To align with these findings, the MW emission analysis is an urgent task that should include targeted detection of inorganic fluorides (HF, POF_3) and fluorinated organics (CH_3F, $C_2H_2F_2$), as well as oxygenated VOCs (acetone, formaldehyde, acrolein).

Beyond their relevance for process optimization, volatile emissions also raise occupational health and safety concerns. Even trace levels of hazardous compounds such as HF, POF_3, formaldehyde, acetaldehyde, and aromatic hydrocarbons may be released during thermal treatment of BM [15, 16]. These substances are corrosive, irritant, or carcinogenic, and chronic exposure, even at concentrations below immediately noticeable thresholds, can pose risks to workers in recycling facilities. Detecting even small amounts is therefore essential, not only to understand decomposition pathways but also to design adequate ventilation, scrubbing, and personal protective strategies for safe large-scale implementation of MW-based recycling. Controlling heating dynamics is therefore not only relevant for maximizing Li recovery but also for minimizing uncontrolled volatile release, which may pose health and safety risks, by using specific abatement technologies. Thus, in order to minimize the formation of inorganic gases, particularly gaseous lithium and volatile fluorine-containing species, a preliminary investigation study of MW conditions was carried out in this work for the first time. A Design of Experiments (DoE) approach was used, followed by statistical multivariate analysis, in order to perform the chemical analysis in the best operating conditions. Thus, the VOCs analysis conducted by solid-phase microextraction (SPME) coupled with gas-chromatography technique was conducted to characterize the volatile profile of real BM samples. A complementary multinuclear NMR analysis, which allowed to confirm specific chemical synthons, is also discussed.

2 | Experimental Part

2.1 | Chemicals

Two batches of industrial BM were considered. The BM1, obtained from grinding LCO and NCM cathodes along with anodic graphite, was provided by Spirit SRL, a local company settled in Vicenza (Italy). The material was subjected to a partial pyrolysis in an industrial environment as a battery pretreatment. BM2 was provided by the Eneris Group, Poland, as a result of a mechanical grinding pretreatment.

2.2 | X-Ray Diffraction (XRD) Analysis

Samples of pristine BM1 and BM2 were analyzed by XRD, employing a Panalytical diffractometer equipped with a Cu Ka (1.5406 Å) radiation source and operating at 40 kV and 40 mA. The patterns were acquired from 10° to 90° (2theta). Both BM showed a crystalline profile in agreement with the already reported ones for similar samples (Figures S7 and S8) [10, 17–19].

2.3 | MW Treatment

Each BM sample (see Table S1) was placed in sealed SPME (20 mL size) vials for headspace analysis and exposed to MW exposure in a Panasonic domestic oven, equipped with an infrared thermometer and a septum quartz crucible. The power of MW and treatment time were settled according to the planned DoE, and the sample was subjected to treatment.

2.4 | Statistical Analysis

A multilevel full factorial DoE was employed to quantify the impact of MW power, processing time, and BM mass on three responses: time needed to reach 600°C, the maximum temperature reached by the system (Tmax), and the amount of Li extracted with a subsequent water leaching. A total number of

TABLE 1 | List of factors and levels.

Factor	Low	Medium	High	Levels	Units
Power	100.0		300.0	2	W
Time	40.0		80.0	3	S
Mass	2.5	4.5	7.5	3	G

18 experiments were carried out (Table S1), while the boundary conditions referred to the considered factors are reported in Table 1.

2.5 | Water Leaching and Li Determination by Ionic Chromatography (IC)

Samples resulting from the 18 experiments reported in Table S1 were subjected to water leaching at 80°C for 30 min with a substrate/leaching agent ratio of 1/20. After filtration of the resulting heterogeneous solution, the water phase was subjected to IC analysis with a dilution factor of 1:100. For IC, a Metrohm 883 Compact IC plus equipped with a cationic exchange Metrosep C4-150/4.0 column.

2.6 | SPME Condition

The BM samples were subjected to SPME coupled with gas chromatography in order to obtain the chemical composition of the VOCs.

The isolation of headspace volatile compounds was carried out using a 50/30 μm PDMS/DVB/CAR (Polydimethylsiloxane/Divinylbenzene/Carboxen) Stableflex, 2 cm fiber (Supelco, Sigma Aldrich, St. Louis, MO, U.S.A.) that was preconditioned according to the manufacturer's instructions. One gram of BM was placed into a 20 mL SPME vial (75.5 × 22.5 mm) that was tightly closed using a septum. After 10 min of equilibration at 60°C, the conditioned fiber was injected through the septum and suspended in the headspace. The fiber was exposed to the volatiles for 10 min; it was then retracted, removed from the vial, and placed immediately into the injector of the GC. Thermal desorption was performed in the injector at a temperature of 240°C for 5 min in splitless injection mode. Prior to and after each analysis, the fiber underwent a further bake-out step for 5 min at 240°C.

As a baseline control, VOCs were analyzed on untreated BM1 and BM2 (i.e., without MW exposure) to quantify the inherent volatile load prior to heating and to discriminate compounds generated during MW processing.

2.7 | Gas Chromatography-Mass Spectrometry (GC-MS) Analysis

The VOCs absorbed by the fiber were subsequently analyzed in a 6890 GC equipped with an Agilent 7673 autosampler and coupled with an Agilent 5973 MSD detector. The chromatographic separation was performed on a Zebron ZB-WAX column 30 m × 0.25 mm i.d., 0.25 μm film thickness column (Phenomenex). The following temperature program was used: 40°C hold for 4 min, then increased to 150°C at a rate of 5.0°C/min, held for 3 min, then increased to 240°C at a rate of 10°C/min, and finally held for 12 min. Helium was used as the carrier gas at a constant flow of 1.0 mL/min. The data were analyzed using a Mass Hunter Workstation B.06.00 SP1, with identification of the individual components (Table S7) performed by comparison against co-injected pure compounds and by matching the MS fragmentation patterns and retention indexes using the built-in libraries, literature data, or commercial mass spectral libraries (NIST/EPA/NIH 2008; HP1607 purchased from Agilent Technologies). A hydrocarbon mixture from C8-C23 was injected under the same HS-SPME/GC-MS conditions to obtain the linear retention indexes.

2.8 | NMR Analyses

Fifty milligrams of BM2 were put in contact with 2 mL of either $CDCl_3$ or D_2O and vigorously shaken to extract soluble compounds. The suspensions were filtered, and the clear solutions transferred to 5 mm NMR tubes. High-resolution liquid-state NMR measurements were performed at 302 K without sample spinning with a Bruker Avance III 400 MHz spectrometer, operating at a magnetic field strength of 9.4 Tesla, equipped with a PABBO probe-head and a variable-temperature unit (^{1}H, ^{7}Li, ^{19}F, and ^{31}P resonance frequencies of 400.13, 155.51, 376.50, and 161.98 MHz, respectively). The instrument was carefully tuned, shimmed, and the 90° pulses were calibrated. 1D ^{1}H spectra were collected with standard Bruker pulse sequences (zg30 for the sample in $CDCl_3$ and noesygppr1d, including water suppression for the sample in D_2O) with 64 scans using 65,536 points over a spectral width of 20 ppm. 1D ^{19}F spectra were collected with 128 scans using 65536 points over a spectral width of 400 ppm. 1D ^{7}Li spectra were collected with 16 scans using 32,768 points over a spectral width of 500 ppm. 1D ^{31}P-{^{1}H} spectra were collected with the standard proton-decoupled Bruker pulse sequences (zgpg30, with waltz16 decoupling scheme) with 2048 scans using 32,768 points over a spectral width of 400 ppm.

3 | Results and Discussion

3.1 | MW Oven Setup

It has been reported that the behavior of the BM under MW exposure reveals a clear onset of the carbothermic reaction once the material reaches around 600°C [10, 19]. At the same time, the heterogeneous composition of the BM and the strong MW absorption of graphite can lead to localized hotspots, which may raise the local temperature well above the measured bulk value. Such conditions have been associated with rapid heating, increased fire risk, and possible lithium losses at elevated temperatures, either through volatilization or transformation into less soluble phases [9]. In this context, a DoE approach was employed to determine the effects of MW power, treatment time, BM mass, and their combinations on the outcome: the time to reach 600°C, the maximum temperature reached by the BM, and the Li extracted during subsequent water leaching. These factors were chosen as they represent the main controllable parameters influencing heating rate, maximum temperature, and Li recovery.

3.1.1 | *Statistical Analysis of the DoE Results for Time_600*

The statistical analysis of the parameters reported in Table 1 in relationship to the time needed to heat the BM at 600°C (Time_600), provided a model with an R^2 of 77,6027%, which explained most of the variance encountered. The standardized Pareto chart, represented in horizontal bars, plots the influences of the factors and their combinations on the selected outcome (Time_600) (Figure 1).

Looking at the Pareto chart in Figure 1, three parameters resulted in determining the Time_600, namely the time, the power, and their linear combination. The bars overcoming the vertical line indicating the p-value < 0.05 are representative with a statistical confidence $> 95\%$.

It is worth noticing that the combination of factors A (power) and B (time) is itself a relevant parameter. This shows a synergistic effect between A and B, suggesting that different powers influence the Time_600 outcome in different ways depending on the time during which the BM is exposed to the MW. The main effects plot and the interaction plot are reported in Figures S1 and S2, respectively. The analysis of the factors showed no influence of the mass of the BM within the considered operational window. The significant Power × Time interaction indicates that higher power accelerates heating, but its effect depends on exposure duration, reflecting the combined influence of instantaneous energy input and bulk thermal inertia. Within the tested range, BM mass did not significantly affect heating time, suggesting that energy absorption was dominated by graphite content and MW coupling efficiency rather than thermal load.

Multiple regression for Time_600 provides the Equation (1).

$$\text{Time\_600} = -50{,}8611 + 0{,}106111 * \text{Power} + 0{,}795833 * \text{time} - 1{,}66667 * \text{mass}. \quad (1)$$

3.1.2 | *Statistical Analysis of the DoE Results for Tmax*

As a result of the statistical analysis related to the Tmax, the R^2 statistic indicates that the model as fitted explains 86,1243% of the variability in Tmax. Pareto chart revealed the predominant influence of time and power, with no relevant effect of the mass or any of the factor's combinations (Figure 2).

The strong dependence on Power and Time, but not on Mass, suggests that peak temperatures are governed by cumulative energy deposition rather than by sample size. Local hotspots likely dominate over bulk heating, which explains why mass has little statistical weight here.

The multiple regression for Tmax is reported in Equation (2).

$$\text{Tmax} = -518{,}639 + 1{,}52667 * \text{Power} + 8{,}725 * \text{time} + 19{,}1667 * \text{mass}. \quad (2)$$

3.1.3 | *Statistical Analysis of the DoE Results for Li*

The ANOVA of the data obtained after water leaching provided a model explaining 67,9457% of the variance. Pareto chart (Figure 3) shows that the amount of Li leached in water is determined by the mass of the BM treated and by the combination of the power and the mass itself. The synergistic AC combination is of particular interest, as it indicates that a determined power of MW exposure influences the carbothermic reduction of the mixed oxides to different degrees depending on the mass of the BM. This combined effect can be related to the amount of graphite, which has a crucial role in participating in the hybrid energy transfer [10, 20]. This interaction reflects the dual role of graphite: as both an MW absorber and a reducing agent. At higher BM masses, graphite availability increases, enhancing carbothermic reduction; however, this benefit is strongly modulated by power level, suggesting a

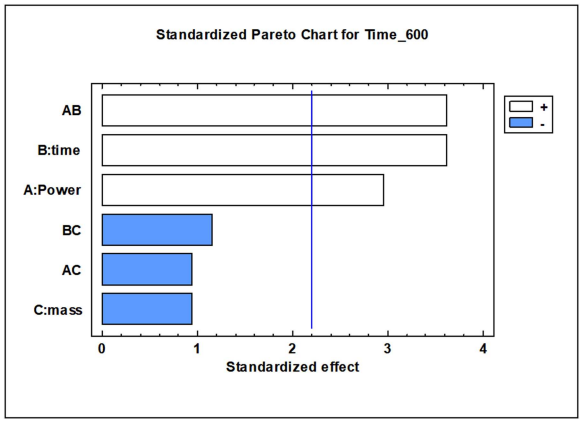

FIGURE 1 | Pareto chart for Time_600. The vertical blue line indicates the threshold of p-value < 0.05.

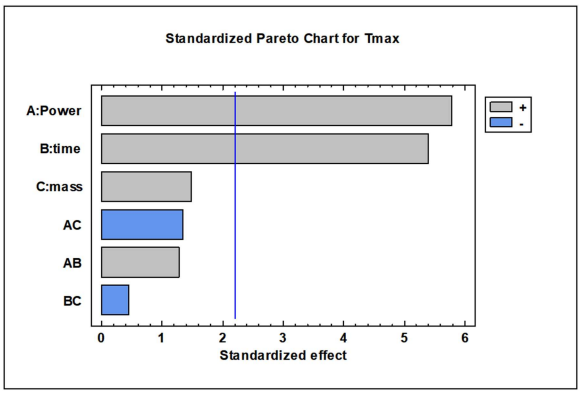

FIGURE 2 | Pareto chart for T-max.

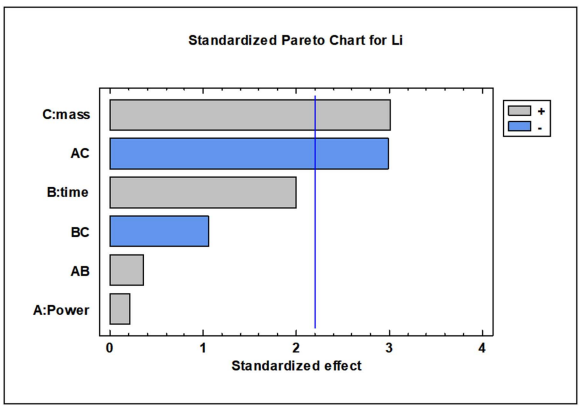

FIGURE 3 | Pareto chart for Li.

threshold in energy transfer efficiency. This effect can be highlighted by looking at the power bar in Figure 3, which is the least impactful on the outcome, while through its interaction with the variation in the mass, it became pivotal in determining the amount of Li leached.

The relatively lower R^2 value for the Li recovery model (~68%) indicates that part of the variability remains unexplained by the chosen factors. This may not only reflect the inherent heterogeneity of the BM and the sensitivity of carbothermic reduction to microstructural differences, but also the analytical steps themselves. Both the water leaching procedure and the subsequent preparation of aliquots for IC can introduce variability, contributing to the observed scatter in the dataset. These limitations highlight that the statistical model captures the main operational trends, but that absolute Li recovery values should be interpreted with caution. Despite these uncertainties, the DoE results clearly reveal the dominant influence of BM mass and its interaction with power, providing a reliable basis for identifying operating windows that enhance Li recovery under MW treatment.

3.1.4 | *Multiple Response Optimization*

Starting from the three models implemented, respectively, for T_600, Tmax, and Li, a desirability function was derived. This was based on the following constraints: increasing Li leaching as much as possible and the maximum temperature, while minimizing the time to reach 600°C. The corresponding plots showing the variation of the desirability function depending on the mass and on the time at fixed values of power are reported (Figure 4a,b).

Looking at the two plots reported in Figure 4, it is possible to notice that exposure at 100 W can be strongly effective depending on the time and the mass. For short times and low masses, this power cannot unlock the conditions needed for the carbothermic reaction required to reach acceptable Li recovery rates. On the other side, for high masses and exposure times above 60 s, it is possible to have a good desirability (Figure 4a). When the power is increased to 300 W, even low masses can be treated in an optimal way in 60 s (Figure 4b). Optimization surfaces highlight that acceptable trade-offs can be achieved at 300 W with moderate BM mass (4–5 g) and exposure times of 60–70 s, balancing rapid heating, controlled Tmax, and enhanced Li recovery. Controlling Tmax and Time_600 not only optimizes Li recovery but also minimizes conditions leading to uncontrolled volatile release (e.g., sudden combustion or fluoride evolution).

3.2 | VOCs Analysis

The multivariate analysis of the data acquired during the experimental plan revealed that the MW processing ideal time was around 1 min (Figure 4), while the effect of the power on the time needed to reach 600°C and on the amount of extracted Li was linked, respectively, to the time (Figure 1) and to the mass (Figure 3). Thus, the first experiments conducted on the BMs consisted of 1 min of MW exposure at two different powers: 100 and 300 W. Then, two BMs, namely BM1 and BM2, were placed in an SPME vial (see Section 2.1) and analyzed by HS-SPME-GC before and after MW (Table 2).

We first established a baseline by analyzing VOCs from untreated BM1 and BM2 (Table 2, samples 1–2; Figure 5). This control confirms that BM2 presents a higher initial VOC burden than BM1, consistent with its lack of prior industrial thermal pretreatment. Subsequent MW exposures (Table 2, samples 3–6) are therefore discussed relative to this baseline.

Looking at the chromatograms of samples 1 and 2, which represent the blanks in the set of experiments reported in Table 2, the first relevant difference was the presence in traces of VOCs in the BM1 with respect to the BM2, which exhibits a significant presence of VOCs (Figure 5).

This different composition in VOCs is in agreement with the origin and processing history of the two materials. In fact, BM1

TABLE 2 | Sample IDs and MW conditions.

ID	Sample	Power (W)	Time (min)
1	BM1	—	—
2	BM2	—	—
3	BM1	100	1
4	BM2	100	1
5	BM1	300	1
6	BM2	300	1

Note: Samples 1–2 correspond to untreated BM1 and BM2 and serve as the baseline control for VOC profiling; samples 3–6 are the same materials after 1 min MW exposure at the indicated power.

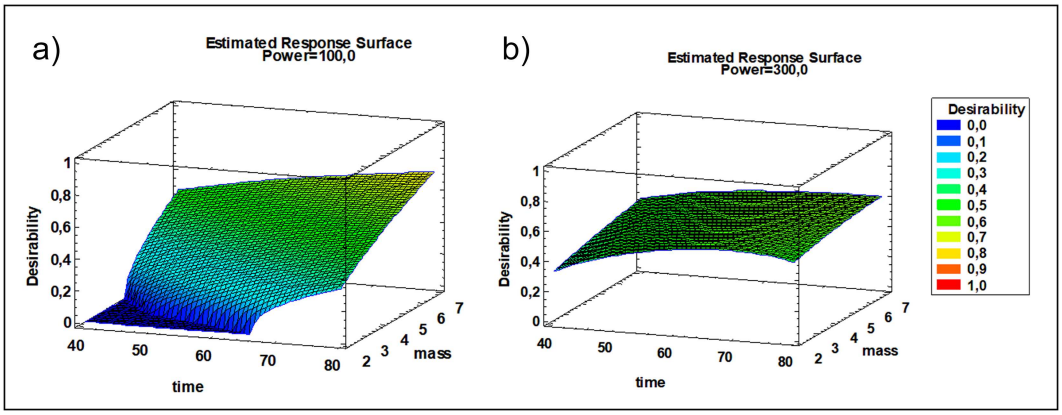

FIGURE 4 | Surface responding plot for power = 100 W (a, left) and power = 300 W (b, right).

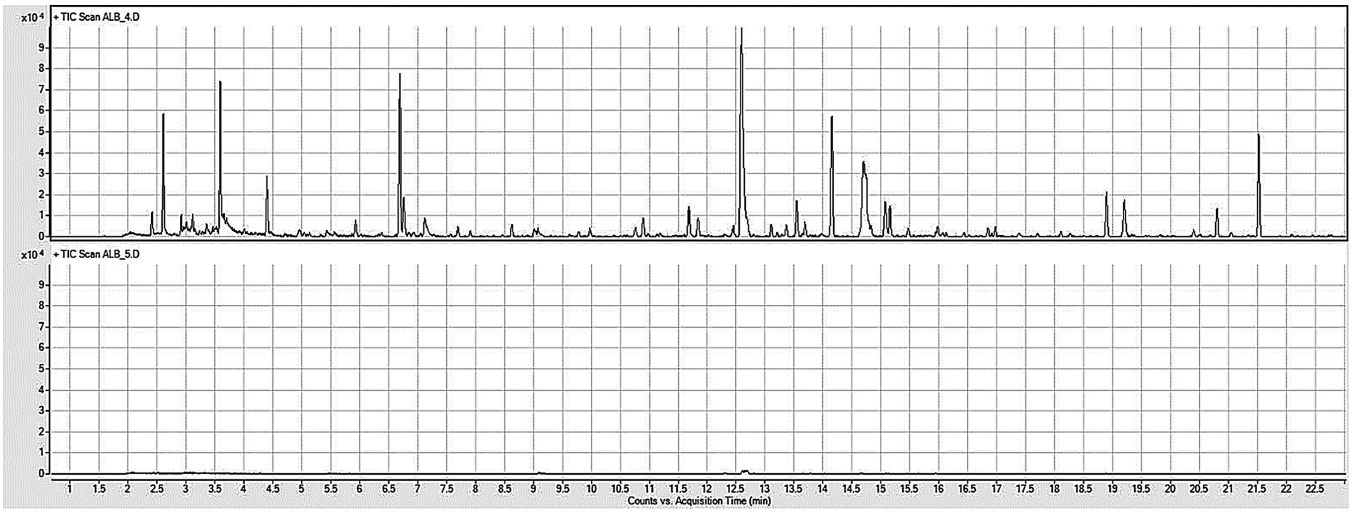

FIGURE 5 | SPME-GC total ion chromatograms (TIC) of 1 (BM1, bottom) and 2 (BM2, up).

had undergone an industrial thermal treatment that removed volatile components, while the POL sample is a raw BM not processed after milling.

Thus, a detailed study on the VOCs emission from BM2, which was processed at 100, 300, 440, 600, and 1000 W (Table S7), was conducted. The analysis of the variation of the VOCs composition at different powers provides a comprehensive view of the chemical transformations occurring during the process. The most statistically significant VOCs whose abundance varies with MW power are reported in Figure 6.

Looking at the data reported in Figure 6, it can be noticed that MW power strongly influences both the amount and the nature of emitted VOCs. The total volatile load increases steadily with power, peaking at 1000 W, which also shows the greatest variability among replicates. Species such as benzaldehyde, acetophenone, styrene, furfural, and several nitriles exhibit strong increases with power, reaching maximum abundance at 1000 W. Conversely, carbonate esters, such as diethyl carbonate, display a consistent decrease, suggesting secondary thermolysis/decarboxylation of EC/DMC-type solvents under heating [21].

From a chemical standpoint, these trends reflect the progressive decomposition of electrolyte and binder components. The enhanced presence of aromatic aldehydes (benzaldehyde) and aromatic ketones (acetophenone) reflects secondary oxidation, cyclization, and aromatization pathways of hydrocarbon fragments during MW exposure, aligning with recent VOCs emission studies from LIB recycling [8]. On the other side, the formation of nitriles and fluorinated olefins, most pronounced at 1000 W, evidences PVDF dehydrofluorination and chain-scission reactions that release HF and volatile fluoro-olefins under thermal treatment [22, 23]. The persistence of phosphate derivatives (triethyl phosphate, dimethyl pentyl phosphate) supports the partial degradation of $LiPF_6$ and the generation of fluorophosphate intermediates and POF_3/fluorophosphate species [24] as widely reported by OEMS/NMR studies [25].

Overall, increasing MW power promotes the transition from moderate VOC release (300–600 W) to intense chemical reorganization (1000 W). This regime, while enhancing lithium recovery, also elevates emissions of aromatics and fluorinated compounds. Hence, process optimization must balance metallurgical efficiency with emission mitigation. Controlling MW power and exposure duration is key to limiting aromatic and fluorinated VOC formation while maintaining effective BM treatment. The data collected at 1000 W (corresponding to local temperatures approaching 1000°C) indicate a clear chemical transition from solvent and binder degradation to secondary condensation and aromatization reactions. At this energy level, the system enters a pyrolytic regime characterized by extensive cracking, dehydration, and cyclization processes, which reshape the volatile profile and lead to the appearance of new high-temperature compounds. At lower powers (300–600 W), most volatile species are light carbonates, short-chain esters, and small oxygenates, typical products of mild thermolysis. At 1000 W, however, secondary pyrolysis reactions dominate, yielding abundant aromatic hydrocarbons (benzaldehyde, acetophenone, styrene), furanic derivatives (furfural, 5-methylfurfural), and nitriles. Several compounds appear exclusively at this power level, confirming the onset of new, high-temperature pathways. These molecules are characteristic of condensation and aromatization pathways occurring under reducing, high-temperature conditions. From a process standpoint, 1000 W represents the transition to a carbonization regime. While this promotes efficient removal of organic binders and enhanced lithium recovery, it simultaneously increases the emission of aromatic and fluorinated VOCs. The detection of fluoro-olefins at high MW power levels is consistent with PVDF binder degradation through dehydrofluorination and chain scission. These reactions release HF and volatile fluorinated fragments, as widely reported in polymer decomposition studies. The presence of these species in the VOC profile confirms PVDF as a primary source of fluorine emissions during MW heating. In addition to library matching, fluorinated species were corroborated by characteristic mass fragments (e.g., CF^+, *m/z* 31; CF_2^+, *m/z* 50; CF_3^+, *m/z* 69) and $PF_3^+/PO_2F_2^+$ clusters, consistent with PVDF dehydrofluorination and $LiPF_6$ decomposition.

3.3 | Multinuclear NMR Analysis

The VOCs analysis revealed the presence of many organic chemicals, especially in the BM2 samples. Even if the interpretation of the GC data is coherent with the origin of the waste

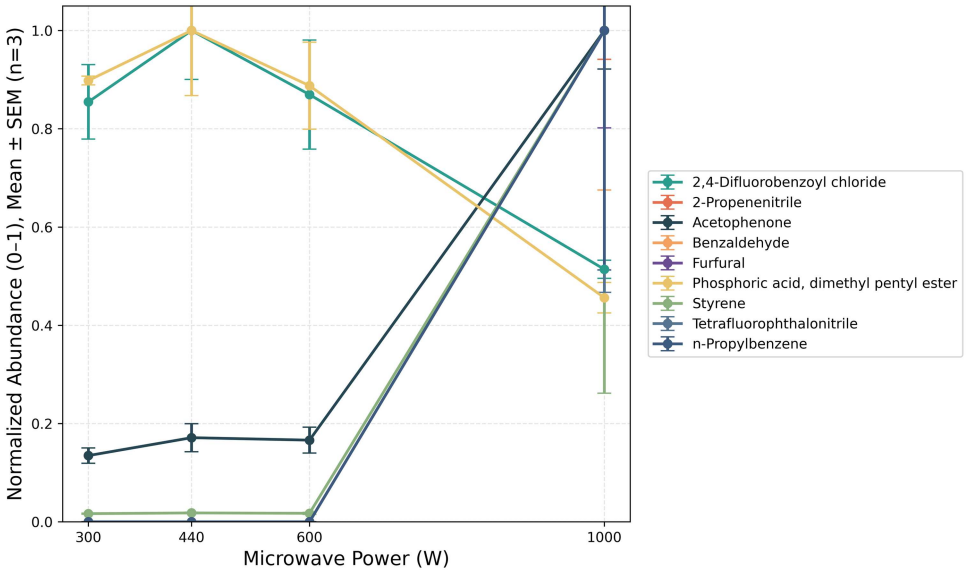

FIGURE 6 | Normalized abundance (0–1) of selected VOCs released from BM2 during microwave treatment as a function of microwave power. Data are reported as mean ± SEM ($n = 3$). Normalization was performed per compound by dividing each value and its SEM by the maximum abundance observed across all powers. VOCs shown: benzaldehyde, styrene, acetophenone, phosphoric acid (dimethyl pentyl ester), 2,4-difluorobenzoyl chloride, n-propylbenzene, 2-propenenitrile, furfural, and tetrafluorophthalonitrile.

TABLE 3 | Qualitative summary of multinuclear NMR analysis of BM2 in $CDCl_3$ and D_2O.

Experiment	D_2O	$CDCl_3$
^{1}H	Aliphatic and aromatic signals from organic compounds	Aliphatic and aromatic signals from organic compounds
^{19}F	Signals of inorganic species	—
^{7}Li	Li^+	—
^{31}P	Signals of inorganic species	—

material, a confirmation about the nature of the detected VOCs by means of a different technique is of high importance to validate the results discussed. In this context, NMR spectroscopy was employed as a complementary technique to get a qualitative fingerprint of the organic compounds contained in BM2. BM samples were extracted directly in deuterated solvents (as reported in Section 2.8), and the clear solutions were analyzed by ^{1}H, ^{31}P, ^{7}Li, and ^{19}F NMR spectroscopy (Table 3). In order to detect the presence of organic or water-soluble chemicals, extractions were performed in both $CDCl_3$ and D_2O.

NMR analysis of BM2 supports the presence of organic and inorganic fractions as detected by HS-SPME-GC partition between polar and apolar extracts. ^{1}H NMR spectra in both D_2O and $CDCl_3$ display a variety of signals distributed in both the aliphatic and aromatic regions (Figure 7a). More in detail, the aliphatic region (Figure 7c) shows marked signals between 0.8 and 2.5 ppm (methyl and methylene protons) together with distinct signals in the 3.0–4.5 ppm region (OCH_2 and OCH_3 protons); these are consistent with electrolyte hydrolysis products and carbonate esters (e.g., EC/DMC derivatives). A few peaks are also observed in the aromatic residues (7–8 ppm, Figure 7b), more markedly in the $CDCl_3$ extract, in agreement with GC identifications of benzaldehyde, styrene, and carbonate esters (Table S7). Together, these observations indicate that polar electrolyte-derived species are partially water-soluble, whereas aromatic hydrocarbons and long-chain esters concentrate in the organic phase, an interpretation that matches the different VOC loads of BM2 versus BM1 discussed earlier.

The multinuclear spectra corroborate the presence of Li-, P-, and F-containing species in aqueous solution. ^{7}Li NMR (Figure 7d) shows a single sharp resonance at roughly $\delta = 0.0$ ppm in the D_2O extract, indicative of solvated Li^+ and compatible with lithium salts originating from the electrolyte and its hydrolysis products. ^{19}F NMR (Figure 7e) exhibits dominant peaks plausibly coming from inorganic species rather than more hydrophobic organofluorines detected by GC, which have limited solubility in D_2O. The singlet at $\delta = -123$ ppm is likely attributable to fluoride species (e.g., LiF in dynamic equilibrium with solvated F^-/HF depending on medium), while the doublet at $\delta = -72$ ppm ($J = 710$ Hz) corresponds to the PF_6^- anion, whose presence is also confirmed in the proton-decoupled ^{31}P NMR spectrum (Figure 7f, septet at $\delta = -145$ ppm, $J = 710$ Hz). Additional resonances between $\delta = -72$ and -79 ppm are detected in the ^{19}F spectrum (Figure 7e). These signals are more plausibly attributed to fluorophosphate species generated by the partial hydrolysis or thermal degradation of $LiPF_6$ (e.g., PO_3F^{2-}, PO_2F^{2-}, or related POF_x intermediates), rather than to organic C—F bonds, which typically resonate much further downfield

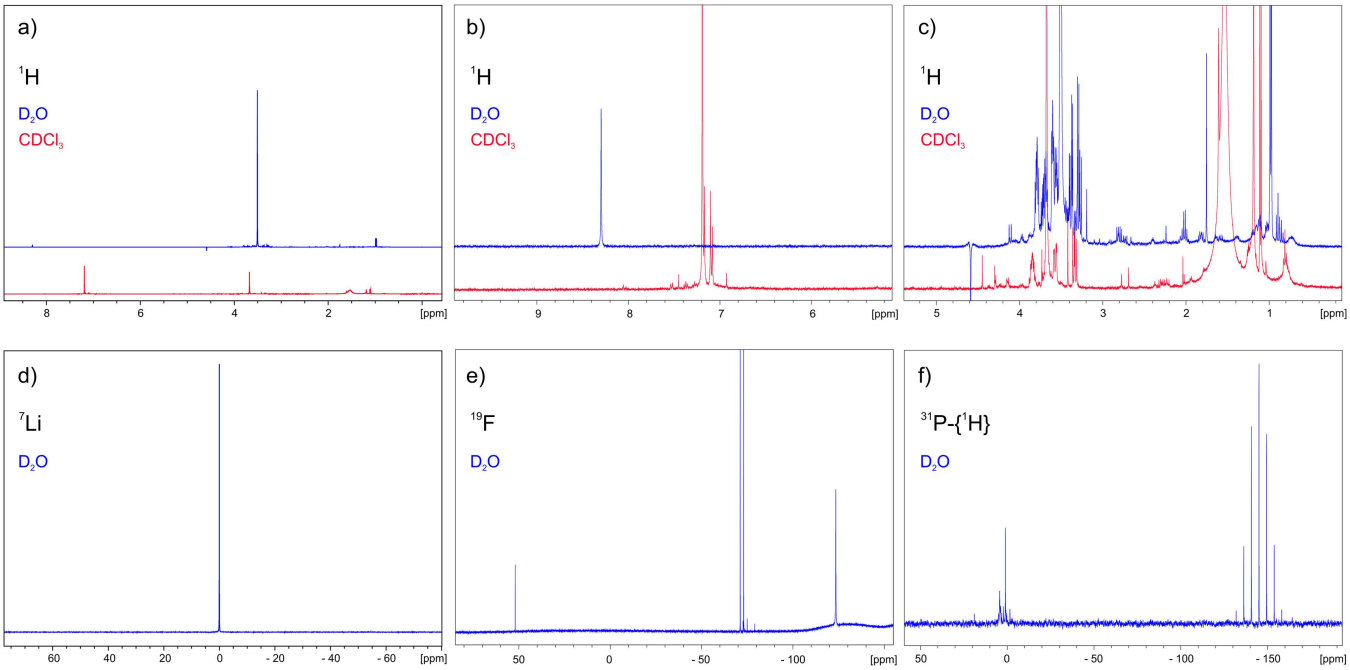

FIGURE 7 | ^{1}H NMR spectrum of BM2 extracts in $CDCl_3$ and D_2O (a) and enlargements of the aromatic (b) and aliphatic (c) regions. ^{7}Li (d), ^{19}F (e), and ^{31}P-{^{1}H} (f) spectra of BM2 extract in D_2O.

(around −110 ppm). Similar chemical shifts for monofluorophosphate and POF_3 have been reported in studies of electrolyte decomposition under humid or oxidative conditions [26, 27]. This interpretation aligns with the ^{31}P-{^{1}H} spectrum (Figure 7f), which shows minor unresolved resonances near 0 ppm compatible with phosphate-type species, supporting the presence of $LiPF_6$-related degradation products in the aqueous extract. A singlet at $\delta = +52$ ppm was occasionally detected in the ^{19}F spectrum; its position may be compatible with gaseous fluorinated species commonly observed as background signals in ^{19}F NMR [22], although its origin cannot be confirmed. ^{19}F and ^{31}P NMR spectra provide direct evidence of electrolyte-derived fluorine species. The PF_6^- resonance and associated fluorophosphate signals (e.g., $PO_2F_2^-$) indicate $LiPF_6$ decomposition pathways leading to POF_3 formation. Together with GC-MS data, these findings clarify that fluorine emissions originate from two distinct sources: PVDF binder and $LiPF_6$ electrolyte, each undergoing specific thermal degradation mechanisms. It should be noted that the BM analyzed in this study had undergone an industrial thermal pretreatment at approximately 600°C–700°C prior to our experiments. As a result, original electrolyte and binder species (e.g., intact PVDF or $LiPF_6$) were largely removed or transformed during this initial step. Therefore, the fluorine-containing compounds detected by GC-MS and NMR represent secondary degradation products rather than pristine cell components. This limitation prevents full characterization of the original sources but does not affect the interpretation of emission pathways during MW heating.

Overall, the NMR data validate the GC assignments and clarify speciation: BM2 retains water- and solvent-soluble electrolyte residues (Li^+, phosphate derivatives, fluoride) alongside non-polar aromatics and esters, reinforcing the interpretation of Table 3 and supporting the VOCs trends reported for the POL series in Table S7.

It should be noted that the BM analyzed represents real industrial waste and has undergone prior processing steps. BM1 was thermally treated at 600°C–700°C, while BM2 was just mechanically shredded. This heterogeneity and unknown initial composition prevent accurate quantification of PVDF and electrolyte content. Therefore, the fluorinated species detected correspond to residual or secondary degradation products rather than pristine cell components. This limitation does not affect the interpretation of emission pathways during MW heating but defines the scope of our conclusions.

3.4 | Final Considerations

Based on the combined statistical outcomes and emission profiles, the most advantageous MW treatment conditions for maximizing lithium recovery while minimizing gaseous emissions correspond to 300 W, 60–70 s, and 4–5 g of BM. Under these conditions, the system achieves sufficiently high local temperatures to trigger partial carbothermic reduction of Li-containing oxides (T_max of about 540°C) without exceeding the threshold (600°C–650°C) where binder and electrolyte residues undergo intense fluorinated gas evolution. According to the dataset in Table S6, this regime can yield Li concentrations up to 24 ppm, while avoiding the steep increase in temperature and volatilization observed beyond 700°C–750°C. These findings are consistent with recent thermal emission studies [23], which show that excessive heating promotes decomposition of carbonate solvents and PVDF into HF, POF_3, and fluoro-olefins. Conversely, maintaining a controlled MW power density and sufficient BM mass stabilizes temperature gradients, preventing local hotspots that favor fluorine release. Therefore, a moderate power/high-mass configuration represents an operational window where Li extraction efficiency and emission safety are jointly optimized. This correlation highlights that the same

experimental factors (power and mass) governing Li recovery also determine the intensity of gas formation, emphasizing the need for integrated optimization of both productivity and environmental performance in MW-based LIB recycling.

4 | Conclusion

This study focused on elucidating the behavior of minor pollutants, particularly VOCs, released during the MW treatment of BM from spent LIBs, under previously optimized and validated operational conditions. Rather than developing a new treatment process, the aim was to clarify how organic and fluorinated species evolve during MW heating and how these findings inform emission monitoring and control strategies in real recycling environments. By applying a multilevel full-factorial DoE, a statistical model was established to describe the influence of MW power, exposure time, and BM mass on key thermal responses (time to 600°C, maximum temperature) and lithium leaching efficiency. This model provides a quantitative and predictive framework for interpreting process behavior, and its structure can be extended to different BM compositions and MW reactor configurations, supporting broader application in industrial-scale recycling setups. The model enables consistent process control and optimization across variable materials and instruments, ensuring reproducibility and safe operation. The detailed characterization of VOCs by HS-SPME/GC–MS, supported by multinuclear NMR spectroscopy, revealed that MW irradiation treatment promotes both the release and secondary transformation of electrolyte- and binder-derived species. Aromatic hydrocarbons, carbonate esters, phosphate derivatives, and fluorinated organics were identified, indicating ongoing decomposition of residual cell components during MW heating. These insights are crucial for understanding pollutant formation and emission mechanisms, providing essential information for future work aimed at assessing and mitigating gaseous releases in recycling environments. Overall, this study demonstrates that MW-assisted pretreatment of BM can simultaneously enhance lithium recovery and mitigate uncontrolled gas evolution when operated within optimized conditions (300 W, 60–70 s, 4–5 g BM). The coupling of DoE-based statistical modeling with chemical speciation analysis establishes a quantitative framework for balancing metallurgical performance and emission control. Future work should include closed-loop MW systems with in-line FTIR or PTR-MS to track HF, POF_3, and VOC formation in real time, enabling adaptive power modulation and safer industrial scale-up.

Acknowledgments

This work was supported by MUR in the frame of the FISA 2022 call, through the project CARAMEL ("New CArbothermic approaches to Recovery criticAL MEtals from spent Lithium-ions batteries" – CUP D73C24000220001). Andrea Mele acknowledges financial support from the Next-GenerationEU (Italian PNRR – M4 C2, Invest 1.3 – D. D. 1551.11-10-2022, PE00000004, CUP D73C22001250001) within the MICS (Made in Italy – Circular and Sustainable) extended partnership. The authors thank Eneris Group and Spirit Srl for the black mass sample supply.

The graphical abstract was realized with BioRender.com. Open access publishing facilitated by Universita degli Studi di Brescia, as part of the Wiley – CRUI-CARE agreement.

Conflicts of Interest

The authors declare no conflicts of interest.

Data Availability Statement

Data are available upon request.

References

1. F. Maisel, C. Neef, F. Marscheider-Weidemann, and N. F. Nissen, "A Forecast on Future Raw Material Demand and Recycling Potential of Lithium-Ion Batteries in Electric Vehicles," *Resources, Conservation & Recycling* 192 (2023): 106920.

2. IEA, Lithium (IEA, 2025), https://www.iea.org/reports/lithium-2.

3. M. Bhar, S. Ghosh, S. Krishnamurthy, Y. Kaliprasad, and S. K. Martha, "A Review on Spent Lithium-Ion Battery Recycling: From Collection to Black Mass Recovery," *RSC Sustainability* 1, no. 5 (2023): 1150–1167.

4. A. Mannu, M. E. Di Pietro, V. Bosello, et al., "Selective and Sustainable Recovery of Lithium From Black Mass via Microwave and Green Leaching Techniques," *Materials Science and Engineering: B* 323, no. B (2026): 118734.

5. A. Cornelio, A. Zanoletti, and E. Bontempi, "Recent Progress in Pyrometallurgy for the Recovery of Spent Lithium-Ion Batteries: A Review of State-of-the-Art Developments," *Current Opinion in Green and Sustainable Chemistry* 46 (2024): 100881.

6. J. P. Harvey, W. Courchesne, M. D. Vo, et al., "Greener Reactants, Renewable Energies and Environmental Impact Mitigation Strategies in Pyrometallurgical Processes: A Review," *MRS Energy & Sustainability: A Review Journal* 9 (2022): 212–247.

7. R. Wang, A. Bulati, L. Zhan, and Z. Xu, "Complicated Pollution Characteristics (Particulate Matter, Heavy Metals, Microplastics, VOCs) of Spent Lithium-Ion Battery Recycling at an Industrial Level," *Science of the Total Environment* 962 (2025): 178406.

8. L. Zhou, F. Ji, Z. Wang, et al., "Emission Characteristics of VOCs From the Typical Spent Lithium-Ion Battery Recycling Industry," *Journal of Hazardous Materials* 493 (2025): 138381.

9. C. Stallmeister, N. Mehl, and B. Friedrich, "Microwave Thermal Treatment of Industrial NMC 622 Lithium-Ion Battery Shredder and Its Influence on Reaction Products Compared to Conventional Pyrolysis," *Journal of Environmental Management* 377 (2025): 124616.

10. A. Cornelio, A. Zanoletti, M. Scaglia, et al., "Thermal Approaches Based on Microwaves to Recover Lithium From Spent Lithium-Ion Batteries," *RSC Sustainability* 2 (2024): 2505–2514.

11. P. Priecel and J. A. Lopez-Sanchez, "Advantages and Limitations of Microwave Reactors: From Chemical Synthesis to the Catalytic Valorization of Biobased Chemicals," *ACS Sustainable Chemistry & Engineering* 7, no. 1 (2019): 3–21.

12. A. Stadler, B. H. Yousefi, D. Dallinger, et al., "Scalability of Microwave-Assisted Organic Synthesis. From Single-Mode to Multimode Parallel Batch Reactors," *Organic Process Research & Development* 7, no. 5 (2003): 707–716.

13. A. Cornelio, E. Galli, M. Scaglia, et al., "Recovery of NMC-Lithium Battery Black Mass by Microwave Heating Processes," *Energy Storage Materials* 72 (2024): 103703.

14. L. S. Gangurde, G. S. J. Sturm, T. J. Devadiga, A. I. Stankiewicz, and G. D. Stefanidis, "Complexity and Challenges in Noncontact High Temperature Measurements in Microwave-Assisted Catalytic Reactors," *Industrial & Engineering Chemistry Research* 56, no. 45 (2017): 13379–13391.

15. F. Larsson, P. Andersson, P. Blomqvist, and P. E. Mellander, "Toxic Fluoride Gas Emissions From Lithium-Ion Battery Fires," *Scientific Reports* 7 (2011): 10018.

16. E. J. K. Nilsson and A. Ahlberg Tidblad, "Gas Emissions From Lithium-Ion Batteries: A Review of Experimental Results and Methodologies," *Batteries* 10, no. 12 (2024): 443.

17. E. Mousa, X. Hu, L. Ånnhagen, et al., "Characterization and Thermal Treatment of the Black Mass From Spent Lithium-Ion Batteries," *Sustainability* 15 (2023): 15.

18. Y.-F. Xia, M. Nie, Z.-B. Wang, et al., "Structural, Morphological and Electrochemical Investigation of $LiNi_{0.6}Co_{0.2}Mn_{0.2}O_2$ Cathode Material Synthesized in Different Sintering Conditions," *Ceramics International* 41, no. 9 (2015): 11815–11823.

19. M. Scaglia, A. Cornelio, A. Zanoletti, et al., "Microwave-Assisted Recovery of Spent $LiCoO_2$ Battery From the Corresponding Black Mass," *Batteries* 9 (2023): 536.

20. M. Bruno, C. Francia, C. Baldo, and S. Fiore, "Selective Recovery of Lithium Carbonate From Lithium-Ion Battery Black Mass Through Microwave-Assisted Carbothermal Reduction and Water Leaching," *Journal of Environmental Management* 393 (2025): 127266.

21. K. Xu, "Nonaqueous Liquid Electrolytes for Lithium-Based Rechargeable Batteries," *Chemical Reviews* 104 (2004): 4303–4418.

22. J. Sharma, C. Totee, V. Kulshrestha, and B. Ameduri, "Spectroscopic Evidence and Mechanistic Insights on Dehydrofluorination of PVDF in Alkaline Medium," *European Polymer Journal* 201 (2023): 112580.

23. Y. Ji, C. T. Jafvert, N. N. Zyaykina, N. Nadezhda, and F. Zhao, "Spectroscopic Evidence and Mechanistic Insights on Dehydrofluorination of PVDF," *Journal of Fluorine Chemistry* 272 (2023): 110044.

24. E. W. C. Spotte-Smith, R. L. Kam, D. Barter, et al., "Toward a Mechanistic Model of Solid–Electrolyte Interphase Formation and Evolution in Lithium-Ion Batteries," *ACS Energy Letters* 7 (2022): 1446–1453.

25. S. Solchenbach, M. Metzger, M. Egawa, H. Beyer, and H. A. Gasteiger, "Quantification of PF_5 and POF_3 From Side Reactions of $LiPF_6$ in Li-Ion Batteries," *Journal of the Electrochemical Society* 165 (2018): A3022–A3028.

26. J. P. Allen and C. P. Grey, "Solution NMR of Battery Electrolytes: Assessing and Mitigating Spectral Broadening Caused by Transition Metal Dissolution," *Journal of Physical Chemistry C* 127, no. 9 (2023): 4425–4438.

27. R. Wagner, M. Korth, B. Streipert, et al., "Impact of Selected LiPF6 Hydrolysis Products on the High Voltage Stability of Lithium-Ion Battery Cells," *ACS Applied Materials & Interfaces* 8, no. 45 (2016): 30871–30878.

Supporting Information

Additional supporting information can be found online in the Supporting Information section.

Figure S1: Main effect plot for Time_600. **Figure S2:** Interaction plot for Time_600. **Figure S3:** Main effects plot for Tmax. **Figure S4:** Interaction plot for Tmax. **Figure S5:** Main effect plot for Li. **Figure S6:** Interaction plot for Li. **Figure S7:** XRD diffractogram of sample MIX_BM. **Figure S8:** XRD pattern for POL_BM sample. **Table S1:** List of experiments and outcomes. **Table S2:** Analysis of Variance for Time_600. **Table S3:** Analysis of the Variance for Tmax. **Table S4:** Analysis of the Variance for Li. **Table S5:** Multiple response optimization boundaries. **Table S6:** Multiple response optimization. **Table S7:** VOCs identified and corresponding absolute integrals with standard deviation (SD).